Suppression of equatorial spread *F* by sporadic *E*

Andrew W. Stephan,[1,2] Marlene Colerico,[3] Michael Mendillo,[3]
Bodo W. Reinisch,[4] and David Anderson[5]

Received 8 June 2001; revised 9 August 2001; accepted 9 August 2001; published 12 February 2002

[1] We have examined quantitatively the influence a low-latitude, premidnight sporadic *E* layer might have on the daily and hourly development of equatorial spread *F* (ESF). In particular, we calculated changes in the flux tube–integrated Pedersen conductivity as it affects the growth rate of the Rayleigh-Taylor instability, which governs the initial development of ESF. We find that the growth rate is lowered by an order of magnitude with a density of 1×10^6 cm^{-3} in a slab from 115 to 120 km. Since sporadic *E* layers observed after dusk do not regularly reach these values, they are not a likely source of the daily variability in ESF. However, even a mild enhancement in the postsunset *E* region could lead to a significant suppression of ESF if it also inhibits the upward plasma drift of the prereversal enhancement, a key variable in the growth rate of the equatorial spread *F* instability. Thus, consistent with the nature of an instability, the second-order effect (suppressed upward drift) is more important than the first-order cause (reduced *F* region to *E* region conductivity) of inhibited ESF onset. *INDEX TERMS:* 2439 Ionosphere: Ionospheric irregularities; 2415 Ionosphere: Equatorial ionosphere; 2447 Ionosphere: Modeling and forecasting

1. Introduction

[2] A new chapter of ionospheric physics was opened with incoherent scatter radar observations of meter-sized equatorial plasma irregularities [*Woodman and LaHoz*, 1976]. *Woodman and LaHoz* [1976] observed these *F* region irregularities associated with the range spread in reflected frequencies seen in radar data. Since then, the term equatorial spread *F* (ESF) has ballooned to encompass instabilities ranging 7 orders of magnitude in size, from centimeters to hundreds of kilometers. A practical need to understand these instabilities has increased as demands on satellite technology and communications systems, such as the Global Positioning System (GPS) network, have grown. Inherent in any requirement of this nature is the ability to predict the development of these relatively common, yet enigmatic, phenomena. A seasonal and longitudinal pattern of ESF occurrence has been observed that is generally consistent with the alignment of the sunset terminator with magnetic field declination [*Tsunoda*, 1985] and the effect of meridional winds which move plasma along field lines both vertically and horizontally [*Maruyama and Matuura*, 1984; *Maruyama*, 1988]. However, these characterizations do not fully represent daily and hourly conditions that govern the occurrence of ESF [*Mendillo et al.*, 1992, 2001]. Thus another factor or factors must contribute to their variability on these time scales.

[3] High parallel conductivity allows the largest ionospheric instabilities, commonly referred to as bubbles, to extend for hundreds of kilometers along a magnetic field line [*Tsunoda*, 1980]. This has the interesting consequence that development of ESF near the equator is controlled by conditions along the flux tube in conjugate hemispheres. Our general understanding of ESF is described by the gravitational Rayleigh-Taylor instability (GRT) [*Ossakow*, 1981; *Kelley*, 1989; *Haerendel et al.*, 1992], where a pocket of lower density plasma percolates up through higher-density plasma via flux tube interchange. The fate of this bubble is determined by the GRT growth rate, γ_{RT}, given by [*Zalesak and Ossakow*, 1982]

$$\gamma_{RT} = \frac{\Sigma_P^F}{\Sigma_P^{E,N} + \Sigma_P^F + \Sigma_P^{E,S}} \left(\mathbf{V}_p - \mathbf{U}_N - \frac{\mathbf{g}}{\nu_{in}} \right) \bullet \frac{\nabla N}{N} - R, \quad (1)$$

where $\mathbf{V}_p$ is the $\mathbf{E} \times \mathbf{B}$ plasma drift velocity, $\mathbf{U}_N$ is the neutral wind, and $\mathbf{g}$ is gravitational acceleration tempered by the ion-neutral collision frequency, ν_{in}. N is the electron density, and R is the chemical recombination rate. Since this is a flux tube interchange instability, all parameters are calculated by integrating local values along the flux tube. The Pedersen conductivity, Σ_P, is also integrated along the flux tube, including contributions from the conjugate north and south *E* regions and the *F* region. Although this approach provides only a lower bound for the growth rate by assuming equipotential field lines [*Rappaport*, 1996], it persists as the primary method for calculating the GRT growth rate [*Haerendel et al.*, 1992; *Sultan*, 1996; *Keskinen et al.*, 1998; *Eccles*, 1998], and thus we use it for our study. In this formulation the *E* region is assumed to be uniform with latitude [*Sultan*, 1996]. Future work should consider the effect a latitudinal gradient in the *E* region will have in further suppressing ESF development.

[4] We have undertaken the task of isolating, for the first time, the effect a nighttime *E* region ionization enhancement would have on the GRT growth rate as a means of evaluating it as a factor in the variability of ESF. In particular, we focus on changes in the Pedersen conductivity ratio in (1) that result from increases in *E* region plasma densities. We have used a simple model of the dusk ionosphere and atmosphere to calculate and compare the Pedersen conductivity ratios for typical and modified *E* region

[1]Formerly at Center for Space Physics, Boston University, Boston, Massachusetts, USA.
[2]Computational Physics, Inc., Springfield, Virginia, USA.
[3]Center for Space Physics, Boston University, Boston, Massachusetts, USA.
[4]Center for Atmospheric Research, University of Massachusetts, Lowell, Massachusetts, USA.
[5]Cooperative Institute for Research in Environmental Sciences and Space Environment Center, NOAA, University of Colorado, Boulder, Colorado, USA.

0148-0227/02/2001JA000162$09.00

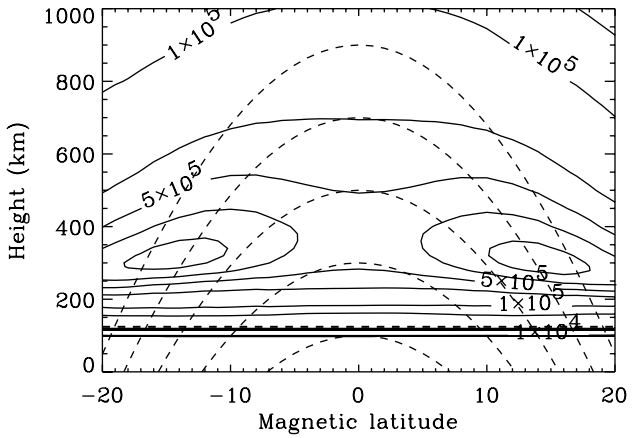

Figure 1. Schematic of dipole field lines and the parameterized ionospheric model (PIM) electron density contours. The horizontal dashed line at 124 km represents the division between the *E* and *F* regions used for these calculations. The thin, flat, artificially modified *E* region slab used in the simulations in Figure 2 falls just below this line.

density profiles. With this framework, we have evaluated the effectiveness of the *E* region in the suppression of ESF on hourly time scales.

2. Model Calculations

[5] We created a meridional slice of the ionosphere and atmosphere near 75°W geographic longitude for the solar-medium conditions of October 1, 1994, using the parameterized ionospheric model (PIM) [*Daniell et al.*, 1995] and the mass spectrometer incoherent scatter (MSIS) E90 model [*Hedin*, 1991]. From the outputs of these models we calculated local Pedersen conductivities and integrated them along all flux tubes with apex heights below 1000 km using a simple dipole model of Earth's magnetic field. Figure 1 shows a schematic of the relative dip latitudes of these field lines superimposed on a 1700 LT ionosphere, including a 1×10^4 cm^{-3} *E* region layer. The complete expression for the flux tube–integrated Pedersen conductivity, Σ_P, uses the expression from *Kelley* [1989] and follows the formulation of *Mendillo et al.* [1992]:

$$\Sigma_P = \int \frac{N_e e^2}{M_i \nu_{in}(1 + k_i^2)} A \, ds, \tag{2}$$

where M_i is the mean ion mass, k_i is the ratio of the ion gyrofrequency to collision frequency, and A is the area of the flux tube at the location, s, along the field line, normalized to a unit area at the magnetic equator. Since PIM does not output ion information, we assumed the plasma is quasineutral and set the ion density equal to the electron density. We approximated M_i with the mean neutral mass calculated from MSIS E90. Although this approach is not explicitly accurate, we will show later that varying ion masses does not significantly alter the results of this calculation, and thus we used this simplifying approximation.

[6] In the postsunset ionosphere where the GRT predominantly occurs, *E* region chemistry proceeds rapidly to reduce the plasma density, and there is no effective contribution to the Pedersen conductivity from these altitudes after around 1800 LT (depending on the local time of sunset in the *E* region). Tsunoda first proposed the modulation of ESF occurrence by E_s layers through their contribution to the flux tube conductivity [see *Sultan*, 1996]. When a sporadic *E* (E_s) layer develops, its contribution to the Pedersen

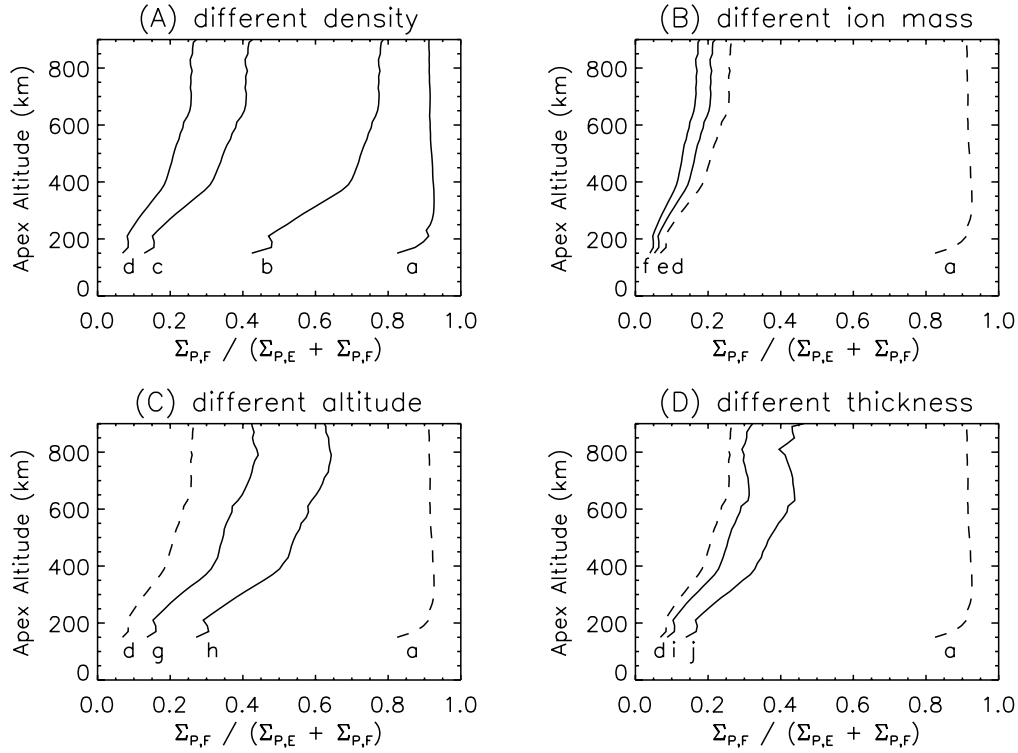

Figure 2. Flux tube–integrated Pedersen conductivity ratio, $\Sigma_P^F/(\Sigma_P^{E,N} + \Sigma_P^F + \Sigma_P^{E,S})$, for various E_s parameters. Curve a is at 1700 LT (where the PIM still predicts an *E* region), while the remaining curves are at 1900 LT. Each plot represents the isolation and modification of one variable in the artificial E_s slab to determine its importance in Σ_P^E and thus the conductivity ratio above. Details for each curve are described in the text and are summarized in Table 1.

conductivity may also become significant. Changes will occur to three parameters in (2) that directly affect the local Pedersen conductivity: N_e, M_i, and ν_{in}. Differences in each of these parameters may exist from case to case depending on the source of the ionization. These changes will compete to enhance or reduce Σ_P^E, modifying the Pedersen conductivity ratio in (1). Thus we isolated each variable and adjusted it to reflect a range of values to determine its significance in changing the GRT growth rate through its influence on this ratio. For each calculation a slab of a particular thickness and altitude was modified to reflect a particular combination of E_s values. All other model outputs were left unchanged. The altitude of separation between *E* and *F* region densities was explicitly determined from the electron density profile.

[7] Our results are plotted in Figure 2 as the conductivity ratio versus flux tube apex height. Each plot corresponds to the adjustment of a different parameter in the artificial E_s layer. The changes to the *E* region for each curve in Figure 2, as will be described in the following text, are summarized in Table 1. The conductivity ratio at 1700 LT is not quite unity because of the small *E* region density ($n_e \sim 1 \times 10^4$ cm^{-3}) in our control run of the model. This ratio is shown as curve a in panel A of Figure 2 for comparison with our remaining results. After 1800 LT this *E* layer disappears and the ratio becomes unity. For subsequent runs we modified our postdusk (1900 LT) ionospheric density between 115 and 120 km. Large decreases in the conductivity ratio are seen at apex heights below 400 km, where ESF onset occurs, as the electron density in the E_s layer is successively raised by 2 orders of magnitude, from 1×10^4 cm^{-3} for curve a to 1×10^6 cm^{-3} for curve d in panel A of Figure 2.

[8] For curves a–d, we assumed the mean ion mass, M_i, to be 56 amu in the slab. The range of ion masses seen in E_s layers initiated by meteor ablation extend from silicon (28 amu) to iron (56 amu) depending on the meteoric composition [*Grebowsky et al.*, 1998]. From (2), smaller M_i will increase Σ_P^E and thus reduce the conductivity ratio in (1). We have explored this in panel B Figure 2 by adjusting M_i in the enhanced slab, from 56 amu seen in curve d, to 40 amu in curve e, and 28 amu in curve f. The effect of this change is small, reducing the conductivity ratio by <0.10.

[9] The decreases in the conductivity ratio shown in panels A and B of Figures 2 will be offset by the ion-neutral collision frequency, ν_{in}, which increases logarithmically with decreasing altitude. Thus a small change in altitude of the low-latitude E_s layers becomes significant. Flux tube–integrated Pedersen conductivities have been shown to change by an order of magnitude between 95 and 125 km [*Tsunoda et al.*, 1994]. In panel C of Figure 2 we have taken the outputs and changes made at 115–120 km to create curve d and lowered the altitude at which those changes have been inserted. Two 5-km drops in altitude, shown in curves g and h, restore the conductivity ratio to >0.25 and as much as 0.60 for flux tubes with higher apex altitudes.

Table 1. E_s Model Parameters

Curve[a]	N_e, cm^{-3}	M_i, amu	Altitude, km
a[b]	...	...	...
b	1×10^5	56	115–120
c	5×10^5	56	115–120
d	1×10^6	56	115–120
e	1×10^6	40	115–120
f	1×10^6	28	115–120
g	1×10^6	56	110–115
h	1×10^6	56	105–110
i	1×10^6	56	115–118
j	1×10^6	56	115–116

[a] Curves are represented in Figure 2.
[b] Curve a uses PIM/MSIS outputs at 1700 LT.

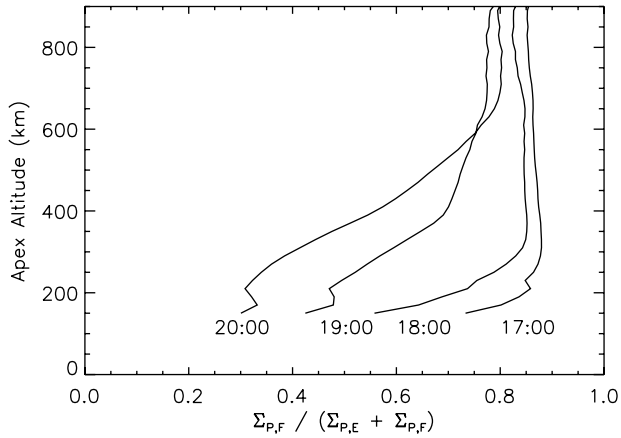

Figure 3. Local time dependence of the effectiveness of a 1×10^5 cm^{-3} E_s layer in reducing the conductivity ratio. The curves at 1700 LT and 1900 LT are the same as curves a and b, respectively, in Figure 2.

[10] Panel D of Figure 2 demonstrates the variability in the conductivity ratio for different E_s layer thicknesses. The thickness of observed E_s layers ranges from a fraction to several kilometers [*Whitehead*, 1989]. Changing the layer in our model from the 5-km-thick slabs in curve d to 3- and 1-km-thick layers, in curves i and j, respectively, only restored the conductivity ratio by a factor of 2 to 0.15 at 200-km apex heights and 0.40 at 800-km apex heights.

[11] As is evident from the runs for 1700 LT and 1900 LT, seen in curves a and b in Figure 2, there will be a significant difference in results for E_s layers appearing at different local times. At later local times, *F* region loss processes will significantly reduce plasma densities from their dusk values. In this scenario the same E_s layer parameters will have a more significant control over the conductivity and thus the growth of ionospheric bubbles and ESF. Figure 3 shows the progression with local time of the influence a 1×10^5 cm^{-3} density enhancement would have (including the results from curves a and b in Figure 2). These curves were obtained as described for Figure 2, superimposing the same modified *E* region density, as described for curve b in Table 1, on the PIM ionosphere produced for each local time. For this comparison we have ignored the additional changes the *E* region would have on the upward plasma drift that is implicit in the PIM. The decay of the *F* region is apparent in the curves, with conductivity ratios progressively dipping to nearly a third of their original value. Thus the timing of the appearance of the E_s layer is significant for its impact on the development of equatorial instabilities.

3. Discussion and Conclusions

[12] Although there is no requirement that our enhanced *E* region densities be due to an E_s layer, we have placed our work in this context. The vertical shear in the meridional wind that is traditionally invoked to explain middle-latitude E_s [*Whitehead*, 1989] becomes less effective at low latitudes where the dip angle is small. Alternative methods require an ionization source such as meteor ablation in the lower ionosphere or precipitation of radiation belt particles in the South Atlantic anomaly (SAA), coupled with either plasma convection to lower latitudes [*Chandra and Rastogi*, 1975] or a vertical shear in the zonal wind [*Abdu and Batista*, 1977]. Low-latitude and equatorial E_s layers with densities estimated to be greater than 1×10^5 cm^{-3} have been observed at local midnight from Cachoeira Paulista, Brazil (22.6°S, 45.0°W; 11.57°S magnetic latitude) [*Batista and Abdu*, 1977]. These ionization enhancements occur in the SAA 1–3 days after a geomagnetic storm and can last for 2–3 hours. Other E_s

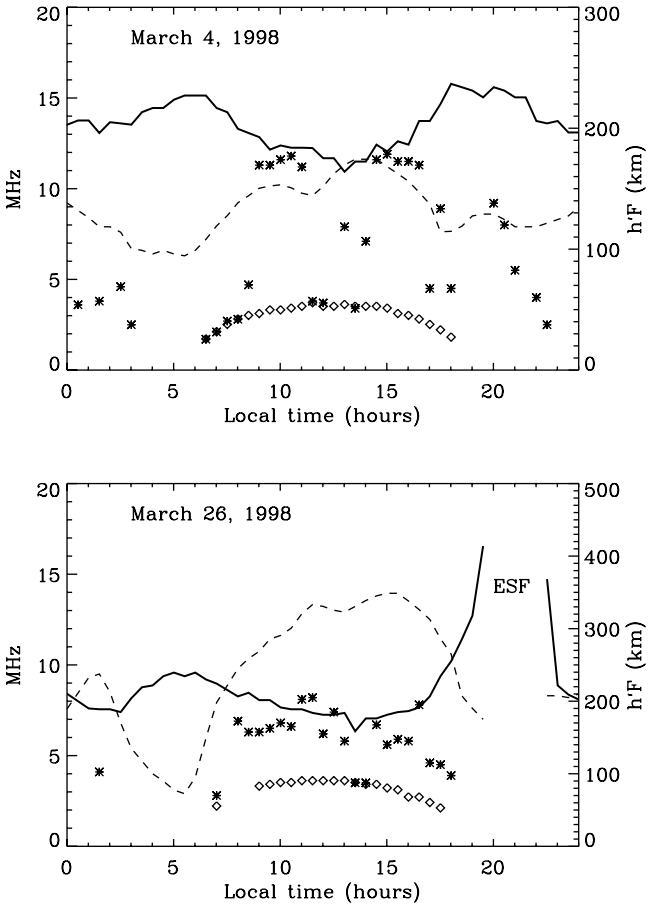

Figure 4. Comparison between two days of Jicamarca ionosonde data: f_oE (diamonds), f_oE_s (asterisks), f_oF_2 (dashed curve), and $h'F$ (solid curve) are shown. For March 4, 1998, no strong spread *F* or scintillation signatures were observed. At 2000 LT, a 10-MHz E_s layer is visible. For March 26, 1998, no E_s layer is present after dusk. However, a strong ESF signature is evident during the gap in f_oF_2 and $h'F$.

layers, with blanketing frequencies exceeding 4 MHz ($\sim 2 \times 10^5$ cm^{-3}), have been seen at night in conjunction with a sodium layer created by meteor ablation [*Batista et al.*, 1989]. Their occurrence increased with local time until midnight and maintained a steady rate between midnight and 0600 LT. The control exhibited by these E_s layers, equal in magnitude to those used in calculating the curves in Figure 3, would map along flux tubes and influence ESF development near 250 km at the magnetic equator. A long-term study (1954–1966) of radar data from Ibadan (7.23°N, 3.9°E geographic; 6°S magnetic latitude) between 1900 and 0500 LT found E_s 40% of the time, with increasing frequency toward later times [*Awe*, 1971]. The average of these years showed a tendency toward minima at equinoxes and maxima at solstices that would reinforce seasonal patterns of ESF, which peak near equinoxes [*Maruyama and Matuura*, 1984; *Tsunoda*, 1985; *Maruyama*, 1988; *Aarons*, 1993]. However, the measured blanketing frequencies rarely exceeded 5 MHz ($\sim 3 \times 10^5$ cm^{-3}). On the basis of this survey of E_s observations, coupled with our simulations, the introduction of a layer that is typically observed would change the conductivity ratio, and thus the GRT growth rate, by less than a factor of 2.

[13] We have compared data from March 4 and March 26, 1998, taken by a Digisonde [*Reinisch*, 1996] at the Jicamarca Radio Observatory (12° S, 77° W; 2° N magnetic latitude). Geomagnetic activity was similar and moderately quiet on both of these days, with $Kp < 4$ and $Dst > -50$ nT. The measured ionospheric frequencies, as well as the virtual height of the *F* layer, $h'F$, are plotted in Figure 4. These two days differ from each other in that March 4 did not exhibit any strong ESF, while March 26 demonstrated the signatures associated with the presence of these instabilities. In particular, the sudden uplift in $h'F$ followed by the gap in observable f_oF_2 and $h'F$ values is characteristic of ESF. In addition, the GPS station in Arequipa, Peru (16°S, 71°W; magnetic dip 3.5°S), recorded strong ESF signatures on March 26 but not on March 4. The GPS phase fluctuation index (F_p) introduced by *Mendillo et al.* [2000] is shown in Figure 5. As described by *Mendillo et al.* [2000] and used in correlative studies by *Mendillo et al.* [2001], F_p values below 50 units signify the absence of ESF, while values 200 and above result from a strong ESF event. Thus by direct measure of ESF on the ionosonde at Jicamarca and by its GPS signatures at Arequipa, we confirm a classic case of day-to-day variability of postsunset ESF during a month of high occurrence rates. Perhaps related to this difference is the strong, 9-MHz ($n_e \sim 1.0 \times 10^6$ cm^{-3}) E_s layer near 2000 LT on March 4. March 26 did not exhibit an evening E_s layer. While a case study covering two nights does not form a definitive link between strong E_s and spread *F*, they do support the conclusions determined by our simulations.

[14] While we have focused on the numerical effect of an E_s layer upon the conductivity term in the growth rate from (1), the results in Figure 4 point to a secondary, and perhaps more important, dynamical influence on the ESF growth rate. The behavior of $h'F$ in Figure 4 shows strong uplifting ($\sim$50 m s^{-1}) on March 26 when *E* region densities were low, and weak uplifting (<10 m s^{-1}) on March 4 when E_s was prominent. The occurrence of the "prereversal enhancement" in vertical plasma drift at the equator in the thermosphere ionosphere electrodynamics general circulation model (TIEGCM) depends critically on the electron density values assigned to the *E* region [*Fesen et al.*, 2000]. *Fesen et al.* [2000] found the critical *E* region density for the development of the prereversal enhancement to be 4×10^3 cm^{-3}. At densities below this value the electrodynamical behavior of the *F* region is set free from *E* region control, while higher densities will short out this independence [see *Kelley*, 1989].

[15] In isolating the Pedersen conductivity for our study, we have ignored several factors that could mitigate or amplify the results shown here. We have performed our calculations away from extremes in solar activity, but flux tube–integrated Pedersen conductivities can vary by as much as a factor of 5 from solar maximum to solar minimum [*Anderson et al.*, 1987]. In addition, we have only modeled conditions for a typical equinox night, and daily and

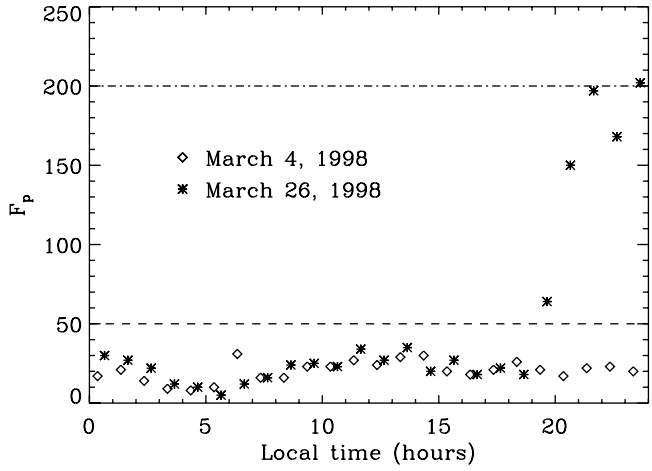

Figure 5. Hourly GPS phase fluctuation index, F_p [*Mendillo et al.*, 2000], for Arequipa, Peru, for March 4 and March 26, 1998. The absence of equatorial spread *F* (ESF) is signified by F_p below 50 (dashed line), while strong ESF is identified by F_p above 200 (dashed-dotted line).

seasonal variations are expected. Finally, although the *F* region does not contribute appreciably to the recombination term, *R*, in (1) [*Huba et al.*, 1996], the *E* region contribution may become significant if an enhanced layer develops. From our model we estimated the recombination resulting from such a layer. If we temporarily ignore the composition of the layer enhancement and use an effective dissociative recombination rate for the primary *E* region constituents, NO^+ and O_2^+, of $\alpha = 2 \times 10^{-7}$ cm^3 s^{-1} [*Rishbeth and Garriott*, 1969], we find that recombination in the enhanced layer can become as significant in controlling the GRT as it is in the dayside *E* region. However, formation of such high-density layers would dictate a smaller recombination rate, closer to the 3×10^{-8} cm ^{3} s^{-1} presumed for a metallic (Mg^+, Fe^+, Si^+) E_s layer [*Abdu and Batista*, 1977]. Thus the effective recombination rate and our calculation of *R*, will be as much as an order of magnitude smaller.

[16] We conclude that E_s layers can change the Pedersen conductivity ratio, and thus the growth rate of ESF, by as much of an order of magnitude. There are three parameters which must be optimized to obtain the maximum effect. First, the magnitude of the change is dependent on the plasma densities in the E_s layer. Second, layers at higher altitudes can take advantage of smaller ion-neutral collision frequencies, leading to a greater reduction in the conductivity ratio. Finally, the effect is larger at later times, when an identical E_s layer will be more influential in the Pedersen conductivity ratio in (1). Composition will play a role primarily in determining recombination rates. However, on the basis of published observations, strong, high-altitude E_s layers having the ability to reduce GRT growth rates via the numerical ratio of *F* region to *E* region Pedersen conductivities appear to be too infrequent to produce the hourly and daily variability in ESF that is observed. A more plausible scenario, one not investigated fully here, has the *E* region enhancement reducing the dominance of the *F* region conductivity, and with it the upward plasma drift. The impact on (1) might be imparted through either a direct change in $\mathbf{V}_p$, a reduction in the height of the *F* region leading to a lower ν_{in}, or both. The multiplicative effect with the change in the Pedersen conductivity ratio could sufficiently reduce the GRT growth rate in (1) and perhaps be one of the keys needed to unlock the mystery of ESF predictability.

[17] **Acknowledgments.** The authors are grateful to Matthew Fox for useful discussions. A.W.S. was supported by Universities Space Research Association STEDI contract 1500-05 and the Massachusetts Space Grant Consortium fellowship 57–528. B.W.R. was supported under Air Force contract F19628-96-0159.

[18] Janet G. Luhmann thanks Peter J. Sultan and Donald Farley for their assistance in evaluating this paper.

References

Aarons, J., The longitudinal morphology of equatorial F-layer irregularities relevant to their occurrence, *Space Sci. Rev.*, *63*, 209–243, 1993.

Abdu, M. A., and I. S. Batista, Sporadic *E* layer phenomena in the Brazilian geomagnetic anomaly: Evidence for a regular particle ionization source, *J. Atmos. Terr. Phys*, *39*, 723–731, 1977.

Anderson, D. N., R. A. Heelis, and J. P. McClure, Calculated nighttime eastward drift velocities at low latitudes and their solar cycle dependence, *Ann. Geophys.*, *5*, 435–442, 1987.

Awe, O., Studies of nighttime E_S at Ibadan near the magnetic equator, *J. Atmos. Terr. Phys.*, *33*, 1209–1222, 1971.

Batista, J. S., and M. A. Abdu, Magnetic storm associated delayed sporadic *E* enhancements in the Brazilian Geomagnetic Anomaly, *J. Geophys. Res.*, *82*, 4777–4783, 1977.

Batista, P. P., B. R. Clemesha, I. S. Batista, and D. M. Simonich, Characteristics of the sporadic sodium layers observed at 23°S, *J. Geophys. Res.*, *94*, 15,349–15,358, 1989.

Chandra, H., and R. G. Rastogi, Blanketing sporadic *E* layer near the magnetic equator, *J. Geophys. Res.*, *80*, 149–153, 1975.

Daniell, R. E., Jr., L. D. Brown, D. N. Anderson, M. W. Fox, P. H. Doherty, D. T. Decker, J. J. Sojka, and R. W. Schunk, Parameterized ionospheric model: A global ionospheric parameterization based on first principles models, *Radio Sci.*, *30*, 1499–1510, 1995.

Eccles, J. V., Modeling investigation of the evening prereversal enhancement of the zonal electric field in the equatorial ionosphere, *J. Geophys. Res.*, *103*, 26,707–26,719, 1998.

Fesen, C. G., G. Crowley, R. G. Roble, A. D. Richmond, and B. G. Fejer, Simulation of the pre-reversal enhancement in the low latitude vertical ion drifts, *Geophys. Res. Lett.*, *27*, 1851–1854, 2000.

Grebowsky, J. M., R. A. Goldberg, and W. D. Pesnell, Do meteor showers significantly perturb the ionosphere?, *J. Atmos. Sol. Terr. Phys.*, *60*, 607–615, 1998.

Haerendel, G., J. V. Eccles, and S. Cakir, Theory for modeling the equatorial evening ionosphere and the origin of the shear in the horizontal plasma flow, *J. Geophys. Res.*, *97*, 1209–1223, 1992.

Hedin, A. E., Extension of the MSIS thermosphere model into the middle and lower atmosphere, *J. Geophys. Res.*, *96*, 1159–1172, 1991.

Huba, J. D., P. A. Bernhardt, S. L. Ossakow, and S. T. Zalesak, The Rayleigh-Taylor instability is not damped by recombination in the *F* region, *J. Geophys. Res.*, *101*, 24,553–24,556, 1996.

Kelley, M. C., *The Earth's Ionosphere*, Academic, Press, San Diego, 1989.

Keskinen, M. J., S. L. Ossakow, S. Basu, and P. J. Sultan, Magnetic flux tube integrated evolution of equatorial ionospheric plasma bubbles, *J. Geophys. Res.*, *103*, 3957–3967, 1998.

Maruyama, T., A diagnostic model for equatorial spread *F*, 1, Model description and application to electric field and neutral wind effects, *J. Geophys. Res.*, *93*, 14,611–14,622, 1988.

Maruyama, T., and N. Matuura, Longitudinal variability of annual changes in activity of equatorial spread *F* and plasma bubbles, *J. Geophys. Res.*, *89*, 10,903–10,912, 1984.

Mendillo, M., J. Baumgardner, X. Pi, P. J. Sultan, and R. Tsunoda, Onset conditions for equatorial spread *F*, *J. Geophys. Res.*, *97*, 13,865–13,876, 1992.

Mendillo, M., B. Lin, and J. Aarons, The application of GPS observations to equatorial aeronomy, *Radio Sci.*, *35*, 885–904, 2000.

Mendillo, M., J. Meriwether, and M. Biondi, Testing the thermospheric neutral wind suppression mechanism for day-to-day variability of equatorial spread *F*, *J. Geophys. Res.*, *106*, 3655–3663, 2001.

Ossakow, S. L., Spread *F* theories: A review, *J. Atmos. Terr. Phys.*, *43*, 437–452, 1981.

Rappaport, H. L., Field line integration and localized modes in the equatorial spread *F*, *J. Geophys. Res.*, *101*, 24,545–24,551, 1996.

Reinisch, B. W., Modern Ionosondes, in *Modern Ionospheric Science*, edited by H. Kohl, R. Rüster, and K. Schlegel, pp. 440–458, European Geophysical Society, Katlenberg-Lindau, Germany, 1996.

Rishbeth, H., and O. K. Garriott, *Introduction to Ionospheric Physics*, Academic Press, San Diego, 1969.

Sultan, P. J., Linear theory and modeling of the Rayleigh-Taylor instability leading to the occurrence of equatorial spread *F*, *J. Geophys. Res.*, *101*, 26,875–26,891, 1996.

Tsunoda, R. T., Magnetic field-aligned characteristics of plasma bubbles in the nighttime equatorial ionosphere, *J. Atmos. Terr. Phys.*, *42*, 743–752, 1980.

Tsunoda, R. T., Control of the seasonal and longitudinal occurrence of equatorial scintillations by the longitudinal gradient in integrated *E* region Pedersen conductivity, *J. Geophys. Res.*, *90*, 447–456, 1985.

Tsunoda, R. T., S. Fukao, and M. Yamamoto, On the origin of quasi-periodic radar backscatter from midlatitude sporadic *E*, *Radio Sci.*, *29*, 349–365, 1994.

Whitehead, J. D., Recent work on mid-latitude and equatorial sporadic *E*, *J. Atmos. Terr. Phys.*, *51*, 401–424, 1989.

Woodman, R. F., and C. LaHoz, Radar observations of *F* region equatorial irregularities, *J. Geophys. Res.*, *81*, 5447–5466, 1976.

Zalesak, S. T., S. L. Ossakow, *On the prospects for artificially inducing equatorial spread F*, *Memo. Rep. 4899*, Naval Research Lab., Washington, D.C., 1982.

D. Anderson, Cooperative Institute of Research in Environmental Sciences, Space Environment Center, NOAA, University of Colorado 325 Broadway, Boulder, CO 80303, USA. (david.anderson@noaa.gov)

M. Colerico and M. Mendillo, Boston University, Center for Space Physics, 725 Commonwealth Ave., Boston, MA 02215, USA. (colerico@bu.edu; mendillo@bu.edu)

B. W. Reinisch, University of Massachusetts Lowell, Center for Atmospheric Research, 600 Suffolk St., Lowell, MA 01854, USA. (Bodo_Reinisch@uml.edu)

A. W. Stephan, Naval Research Laboratory, Code 7643, 4555 Overlook Ave. SW, Washington, D. C. 20375, USA. (stephan@uap2.nrl.navy.mil)